SCIENCE CHINA
Technological Sciences

•Article•

March 2022 Vol.65 No.3: 541–552
https://doi.org/10.1007/s11431-021-1955-8

A modified similitude analysis method for the electro-mechanical performances of a parallel manipulator to solve the control period mismatch problem

WU Jun[1,2*], SONG YuYao[1,2], LIU ZiLin[1,2] & LI GuoFa[3]

[1] *State Key Laboratory of Tribology and Institute of Manufacturing Engineering, Department of Mechanical Engineering, Tsinghua University, Beijing 100084, China;*
[2] *Beijing Key Lab of Precision/Ultra-precision Manufacturing Equipment and Control, Beijing 100084, China;*
[3] *Key Laboratory of CNC Equipment Reliability, Ministry of Education, Jilin University, Changchun 130022, China;*

Received September 19, 2021; accepted November 1, 2021; published online December 20, 2021

Due to the discrete feature and performance limitation of the numerical controller, the control period sometimes cannot meet the constraints of the scaled model in similitude analysis, which brings the control period mismatch problem. The traditional similitude analysis methods are not able to solve this problem since the controller is treated as continuous system in these methods. This paper proposes a modified similitude analysis method to solve the control period mismatch problem, and the electro-mechanical performances of a 2-DOF parallel manipulator is predicted. Based on the model of dynamic and control system, most of the similitude laws are derived by taking the controller as continuous system. Then the transfer function of the controller in discrete form is established, and the similitude law related to control period is derived to figure out the cause of mismatch problem. The modified method, named long period equivalent, is proposed to solve the mismatch problem by using the least square method and superposition principles. Finally, the scaled model of the parallel manipulator is determined based on the modified similitude analysis method.

similitude analysis, control period mismatch, parallel manipulator, electro-mechanical performance, discrete system

Citation: Wu J, Song Y Y, Liu Z L, et al. A modified similitude analysis method for the electro-mechanical performances of a parallel manipulator to solve the control period mismatch problem. Sci China Tech Sci, 2022, 65: 541–552, https://doi.org/10.1007/s11431-021-1955-8

1 Introduction

From the viewpoint of mechanism, the mechanism can be divided into serial mechanism and parallel mechanism [1]. Each mechanism has its advantages and disadvantages [2]. From the viewpoint of machine tool development, both serial mechanisms and parallel mechanisms can be used to design machine tools. However, the hybrid mechanism that combines the serial mechanism and parallel mechanism is the ideal configuration for a machine tool [3,4]. Thus, some hybrid machine tools such as Exechon, Trimule and Tricept are developed for industrial application [5–7].

The hybrid machine tool is a typical electro-mechanical equipment and the electro-mechanical dynamic performances are complex. It is a challenge to accurately predict the electro-mechanical performances. Although the modelling approaches of the electro-mechanical coupling dynamics have been widely studied, most of them concentrate on single axis or certain component of the manipulators [8–11]. Therefore, the test and experiment on the prototype of hybrid machine tool is still necessary to validate the predicted performances [12,13]. However, it is difficult to perform the experimental study on the full-size prototypes of heavy-duty machine tools due to the huge economic cost,

*Corresponding author (email: jhwu@mail.tsinghua.edu.cn)

long manufacturing time and high security risk.

Fortunately, an alternative method to replace the performance test on full-size prototype, named scaled down experiment based on the similitude principles, can be used to estimate the performance of a hybrid machine tool. A scaled model that is proportionally scaled down in size is tested in the scaled down experiment [14]. The key issue of scaled down experiment, called similitude analysis, is to establish the quantitative relationships between the full-size prototype and scaled model. Based on the similitude analysis, the performance of full-size prototype can be accurately predicted by designing a proper scaled model.

The traditional scaled down experiment and similitude analysis [15–18] mainly focus on the systems with single energy type and a few variables [19,20]. Now, the similitude analysis is expanded to electro-mechanical coupling systems with multi energy types and a lot of variables [21]. The controllers are regarded as continuous system to simplify the similitude analysis, and the performance can be accurately predicted if the gain of controller is relatively low. However, the actual controllers are usually discrete and the mismatch of control period will occur if the controller gain is relatively high. This problem will lead to inaccurate prediction or even unstable oscillation of the scaled model. Therefore, it is necessary to consider the problem of control period mismatch to study the similitude analysis method of electro-mechanical system.

In this paper, the similitude analysis of electro-mechanical performances of a 2-DOF parallel manipulator is investigated. The controller in discrete form is established to derive the similitude law related to control period, so that the cause and effects of mismatch problem can be clearly figured out. A long period equivalent (LPE) method is proposed to deal with the control period mismatch. Experiments on the scaled model of the parallel manipulator are carried out to validate the LPE.

2 2-DOF parallel manipulator in a hybrid machine tool

As shown in Figure 1, a heavy-duty hybrid machine tool with 5-DOF is designed to mill huge blades and guide vanes for hydraulic turbines. The machine tool is composed of a 2-DOF parallel manipulator, a 2-DOF tool head and a feed worktable. The 2-DOF parallel manipulator consists of two parallelogram kinematic chains, two active sliders, a moving platform and a gantry frame. The ends of each kinematic chain are connected to a slider and the moving platform by revolute joints, respectively, while the sliders are driven by ball screws which are directly connected to servo motors. The moving platform can move along the vertical and horizontal directions.

Although the full-size experiments on physical prototype of heavy-duty manipulator can be used to accurately predict the manipulator performances, it will take a long time and high cost to manufacture the full-size parallel manipulator. In this paper, the scaled down experiment and similitude analysis are used to predict the tracking performances of the 2-DOF parallel manipulator. The full-size prototype and scaled model have a similar kinematic model and the kinematic model is derived for the similitude analysis. The schematic diagram of the parallel manipulator is shown in Figure 2.

In Figure 2, *o-xy* is the global coordinate system fixed on the gantry frame, and *O-XY* is the local coordinate system fixed on the center of the moving platform. The closed-loop vector equation can be written as

$$\begin{cases} \mathbf{r} = \dfrac{d-b}{2}\mathbf{e}_v + q_1\mathbf{e}_h + l_k\mathbf{e}_{l1}, \\ \mathbf{r} = \dfrac{b-d}{2}\mathbf{e}_v + q_2\mathbf{e}_h + l_k\mathbf{e}_{l2}, \end{cases} \tag{1}$$

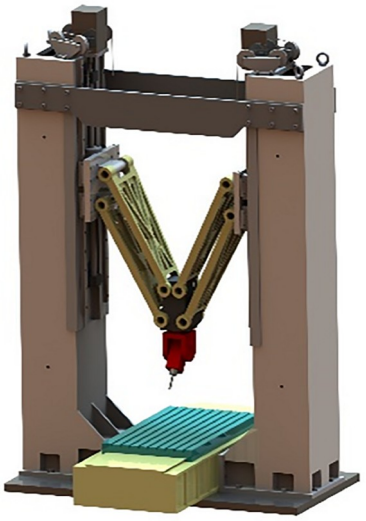

Figure 1 (Color online) 5-DOF heavy-duty hybrid machine tool.

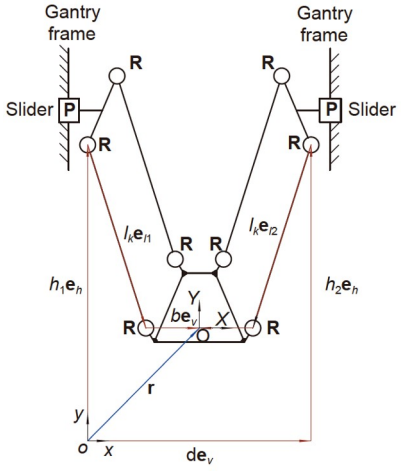

Figure 2 (Color online) Schematic diagram of the parallel manipulator.

where $\mathbf{r}$ is the vector from o to O, $\mathbf{e}_h$ is the unit vector along x direction, and $\mathbf{e}_v$ is the unit vector along y direction. $\mathbf{e}_{l1}$ and $\mathbf{e}_{l2}$ are unit vectors along the axes of each link. d is the distance between two ball screws. q_1 and q_2 are the position of two sliders along the ball screws. b is the width of the moving platform and l_k is the length of each link. Among all the parameters, q_1, q_2, $\mathbf{r}$ and the directions of $\mathbf{e}_{l1}$ and $\mathbf{e}_{l2}$ are variables. Based on eq. (1), q_1 and q_2 can be obtained with a given $\mathbf{r}$.

3 Similitude analysis of the parallel manipulator

In similitude analysis, it is important to establish the corresponding similitude laws, which are defined as a group of invariants between the full-size prototype and scaled model. Since some similitude laws related to the electro-mechanical performances are shared by both continuous and discrete systems, the shared similitude laws are derived in this section, and then the rest similitude laws will be derived in Section 4 by considering the characteristics of discrete systems.

The parallel manipulator is an electro-mechanical coupling system and it is divided into dynamic and control subsystems. The similitude analysis of each subsystem is carried out firstly, and then the coupling relationships are considered to complete the similitude analysis of the whole electro-mechanical coupling system.

3.1 Similitude analysis of dynamic system

The dynamic equation of the parallel manipulator in Cartesian space can be expressed as

$$\mathbf{M}\ddot{\mathbf{r}}+\mathbf{C}\dot{\mathbf{r}}+\mathbf{f}_g=\mathbf{f}, \tag{2}$$

where $\mathbf{M}$, $\mathbf{C}$ and $\mathbf{f}_g$ are inertia matrix, centrifugal/Coriolis force matrix and gravity vector, and $\mathbf{f}$ is the external force. $\mathbf{M}$, $\mathbf{C}$ and $\mathbf{f}_g$ are all proportional to material density ρ, namely

$$\mathbf{M}=\rho\widetilde{\mathbf{M}},\ \mathbf{C}=\rho\widetilde{\mathbf{C}},\ \mathbf{f}_g=\rho\tilde{\mathbf{f}}_g, \tag{3}$$

where $\tilde{\mathbf{f}}_g$ is proportional to the gravitational acceleration g and $\mathbf{f}_g=\rho g\begin{bmatrix}0 & 0 & m_g\end{bmatrix}^{\mathrm{T}}$. Thus, the dynamic equation in joint space can be expressed as

$$\mathbf{M}_q\ddot{\mathbf{q}}+\mathbf{C}_q\dot{\mathbf{q}}+\mathbf{f}_{gq}=\mathbf{f}_q, \tag{4}$$

where $\mathbf{M}_q=\mathbf{J}_q^{\mathrm{T}}\mathbf{M}\mathbf{J}_q$, $\mathbf{C}_q=\mathbf{J}_q^{\mathrm{T}}\mathbf{C}\mathbf{J}_q$, $\mathbf{f}_{gq}=\mathbf{J}_q^{\mathrm{T}}\mathbf{f}_g$, $\mathbf{f}_q=\mathbf{J}_q^{\mathrm{T}}\mathbf{f}$, $\mathbf{q}=[q_1\ \ q_2]^{\mathrm{T}}$, and $\mathbf{J}_q$ is the Jacobian matrix from joint space to Cartesian space. Based on eq. (1), $\mathbf{J}_q$ can be expressed as

$$\mathbf{J}_q=\begin{bmatrix}\dfrac{\partial\mathbf{r}}{\partial q_1} & \dfrac{\partial\mathbf{r}}{\partial q_2}\end{bmatrix}.$$

All parameters related to the dynamic system are included in eqs. (1) and (4). Taking the dimensions of length, mass and time as the basic dimensions, the dimensions of all parameters in eq. (4) can be classified, as shown in Table 1. In Table 1, [*] represents the dimension of parameter *, and $\mathbf{l}$ represents the set that consists of all geometric parameters corresponding to the dynamic system. From eq. (1), it can be known that b, d and l_k are included in this set. By filling the data in Table 1 into the corresponding position of a 3×13 matrix, it can be derived that the rank of this matrix is 3. Based on dimensional analysis method and Table 1, the amount of independent dimensions related to dynamic characteristics is 3, and the number of similitude laws is 10. These similitude laws can be written as

$$\begin{aligned}&\boldsymbol{\pi}_1=\frac{\widetilde{\mathbf{M}}}{\mathbf{l}^3},\ \boldsymbol{\pi}_2=\frac{\widetilde{\mathbf{C}}}{g^{0.5}\mathbf{l}^{2.5}},\ \boldsymbol{\pi}_3=\frac{\mathbf{f}}{\rho g\mathbf{l}^3},\ \boldsymbol{\pi}_4=\mathbf{q},\\&\boldsymbol{\pi}_5=\frac{\dot{\mathbf{q}}}{g^{0.5}\mathbf{l}^{-0.5}},\ \boldsymbol{\pi}_6=\frac{\ddot{\mathbf{q}}}{g\mathbf{l}^{-1}},\ \boldsymbol{\pi}_7=\frac{t}{g^{-0.5}\mathbf{l}^{0.5}},\\&\boldsymbol{\pi}_8=\frac{\mathbf{J}_q}{\mathbf{l}},\ \boldsymbol{\pi}_9=\frac{m_g}{\mathbf{l}^3},\ \boldsymbol{\pi}_{10}=\frac{\mathbf{r}}{\mathbf{l}}.\end{aligned} \tag{5}$$

It should be noticed that $\boldsymbol{\pi}_i(i=1,\ldots,10)$ in eq. (5) denotes a group of similitude laws. Besides, to avoid distortion of dynamic system, the geometric shape of the full-size prototype and scaled model should be the same. Thus, the following similitude laws are satisfied:

$$\boldsymbol{\pi}_{11}=\frac{b}{d},\ \boldsymbol{\pi}_{12}=\frac{b}{l_k}. \tag{6}$$

Moreover, based on the definition of similitude laws, the constraints of scaling ratios between the scaled model and full-size prototype related to dynamic characteristics can be derived as

$$\begin{aligned}&\lambda_{\widetilde{\mathbf{M}}}=\lambda_{\mathbf{l}}{}^3,\ \lambda_{\widetilde{\mathbf{C}}}=\lambda_g{}^{0.5}\lambda_{\mathbf{l}}{}^{2.5},\ \lambda_{\mathbf{f}}=\lambda_g\lambda_{\mathbf{l}}{}^3\lambda_\rho,\ \lambda_{\mathbf{q}}=1,\\&\lambda_{\dot{\mathbf{q}}}=\lambda_g{}^{0.5}\lambda_{\mathbf{l}}{}^{-0.5},\ \lambda_{\ddot{\mathbf{q}}}=\lambda_g\lambda_{\mathbf{l}}{}^{-1},\ \lambda_t=\lambda_g{}^{-0.5}\lambda_{\mathbf{l}}{}^{0.5},\\&\lambda_{\mathbf{J}_q}=\lambda_{\mathbf{l}},\ \lambda_{m_g}=\lambda_{\mathbf{l}}{}^3,\ \lambda_{\mathbf{r}}=\lambda_{\mathbf{l}},\ \lambda_b=\lambda_d,\lambda_b=\lambda_{lk}.\end{aligned} \tag{7}$$

Table 1 Dimensions of parameters related to dynamic system

	$[\widetilde{\mathbf{M}}]$	$[\widetilde{\mathbf{C}}]$	$[g]$	$[\mathbf{f}]$	$[\mathbf{r}]$	$[\mathbf{q}]$	$[\dot{\mathbf{q}}]$	$[\ddot{\mathbf{q}}]$	$[t]$	$[\mathbf{J}_q]$	$[m_g]$	$[\rho]$	$[\mathbf{l}]$
$[L]$	3	3	1	1	1	0	0	0	0	1	3	−3	1
$[M]$	0	0	0	1	0	0	0	0	0	0	0	1	0
$[t]$	0	−1	−2	−2	0	0	−1	−2	1	0	0	0	0

Let a' and a be the value of the parameter in scaled model and full-size prototype, respectively. $\lambda_a = \frac{a'}{a}$ represents the scaling ratio of a. In engineering practice, the material used in the scaled model is usually the same as that of the full-size prototype. Thus, $\lambda_\rho = 1$. Moreover, since the scaled model and the full-size prototype are in the same gravity field, it can be obtained that $\lambda_g = 1$. Therefore, eq. (7) can be rewritten as

$$\begin{aligned}&\lambda_{\widetilde{\mathbf{M}}} = \lambda_{\mathbf{l}}^3,\ \lambda_{\bar{\mathbf{C}}} = \lambda_{\mathbf{l}}^{2.5},\ \lambda_{\mathbf{f}} = \lambda_{\mathbf{l}}^3,\ \lambda_{\mathbf{q}} = 1,\ \lambda_{\dot{\mathbf{q}}} = \lambda_{\mathbf{l}}^{-0.5},\\ &\lambda_{\ddot{\mathbf{q}}} = \lambda_{\mathbf{l}}^{-1},\ \lambda_t = \lambda_{\mathbf{l}}^{0.5},\ \lambda_{\mathbf{J}_q} = \lambda_{\mathbf{l}},\ \lambda_{m_g} = \lambda_{\mathbf{l}}^3,\ \lambda_{\mathbf{r}} = \lambda_{\mathbf{l}},\\ &\lambda_b = \lambda_d,\ \lambda_b = \lambda_{lk}.\end{aligned} \tag{8}$$

In eq. (8), only one scaling ratio is independent. For convenience, $\lambda_{\mathbf{l}}$ is usually selected as the independent scaling ratio, while the others are determined based on $\lambda_{\mathbf{l}}$ and eq. (8).

3.2 Similitude analysis of control system

Closed-loop feedback plus velocity feedforward control is used for the parallel manipulator. The position loop is a P controller while the velocity loop is a P-I controller. Due to the fast response of current loop, its transfer function is approximately regarded as 1. The characteristic equation of the closed loop transfer function can be derived as

$$G = J_m s^3 + K_t K_v s^2 + K_t\left(I_v + K_p K_v\right)s + K_p K_t I_v,$$

where s is the complex frequency, K_t is the moment constant, J_m is the moment of inertia of the motor, and K_p, K_v and I_v are proportional coefficient of the position loop, proportional coefficient and integral coefficient of the velocity loop, respectively. Based on the Routh criterion, the control parameters satisfy $\frac{K_v K_t\left(I_v + K_p K_v\right)}{K_p I_v} > J_m$ if the controller is stable.

Based on the equation analysis method in complex frequency domain [22], the similitude laws related to control system are derived by selecting each block as the basic unit of analysis.

$$\begin{aligned}&\boldsymbol{\pi}_{13} = \frac{s\theta_c K_{\mathrm{vff}}}{\dot{\theta}},\ \boldsymbol{\pi}_{14} = \frac{\theta_c K_p}{\dot{\theta}},\ \boldsymbol{\pi}_{15} = \frac{\dot{\theta} I_v}{s i},\ \boldsymbol{\pi}_{16} = \frac{\dot{\theta} K_v}{i},\\ &\boldsymbol{\pi}_{17} = \frac{i K_t}{\tau},\ \boldsymbol{\pi}_{18} = \frac{\tau_o}{\tau},\ \boldsymbol{\pi}_{19} = \frac{\tau}{J_m \ddot{\theta}},\ \boldsymbol{\pi}_{20} = \frac{\ddot{\theta}}{s\dot{\theta}},\\ &\boldsymbol{\pi}_{21} = \frac{\dot{\theta}}{s\theta},\ \boldsymbol{\pi}_{22} = \frac{\theta_c}{\theta},\end{aligned} \tag{9}$$

where θ_c and θ are the command and actual angular position of the motor, τ and τ_o are the driving torque and external torque, and K_{vff} is the velocity feedforward coefficient. Eq. (9) illustrates the similitude laws related to control characteristics. Based on eq. (9) and the relationship between the scaling ratio of s and t, the constraints of the scaling ratios related to control system can be expressed as

$$\begin{aligned}&\lambda_{\theta c}\lambda_{K\mathrm{vff}} = \lambda_t\lambda_{\dot{\theta}},\ \lambda_{\theta c}\lambda_{Kp} = \lambda_{\dot{\theta}},\ \lambda_i\lambda_{Kt} = \lambda_\tau,\ \lambda_{\tau o} = \lambda_\tau,\\ &\lambda_{\dot{\theta}}\lambda_{Iv}\lambda_t = \lambda_i,\ \lambda_{\dot{\theta}}\lambda_{Kv} = \lambda_i,\ \lambda_{Jm}\lambda_{\ddot{\theta}} = \lambda_\tau,\ \lambda_t\lambda_{\ddot{\theta}} = \lambda_{\dot{\theta}},\\ &\lambda_t\lambda_{\dot{\theta}} = \lambda_\theta,\ \lambda_{\theta c} = \lambda_\theta.\end{aligned} \tag{10}$$

From the relationships between the dynamic and control systems in Section 3.3, it will be clarified that only one scaling ratio in eq. (10) is independent. Therefore, in practical application, λ_{Kt} is usually settled as the independent one to select the motors. It should be noticed that the control characteristics of each axis in a multi-axis system should satisfy eq. (10) no matter what the control parameters are.

3.3 Similitude analysis of the electro-mechanical coupling system

The dynamic and control system are coupled through angular position and driving torque, and the coupling constraints can be expressed as

$$nq = \theta,\ f_q = n\tau_o, \tag{11}$$

where n is the reduction ratio of the mechanism. Let q_d be the lead of the screw. It can be concluded that n equals $\frac{2\pi}{q_d}$ since the motor is directly connected to the ball screw. Based on the coupling constraints in eq. (11), the additional scaling laws can be derived as

$$\boldsymbol{\pi}_{23} = \frac{nq}{\theta},\ \boldsymbol{\pi}_{24} = \frac{f_q}{n\tau_o}. \tag{12}$$

Based on eq. (12), the corresponding constraints of the scaling ratios can be derived as

$$\lambda_n\lambda_q = \lambda_\theta,\ \lambda_{fq} = \lambda_n\lambda_{\tau o}. \tag{13}$$

For each axis of the parallel manipulator, eq. (13) is satisfied. Moreover, eq. (13) shows the connections between the dynamic and control systems. It can be concluded that the amount of independent scaling ratio in eq. (10) is only 1.

Eqs. (5), (6), (9) and (12) are the similitude laws for the continuous electro-mechanical system. If they are directly used to investigate the similarity of discrete system, it will bring the problem of control period mismatch in high control gain condition which will be discussed in the next section.

4 The problem of control period mismatch

In engineering application, the control system usually works in numerical mode. The control algorithm is calculated on discrete time series and the output signal is discontinuous. Therefore, the actual controller is essentially a discrete system. Compared with continuous system, the discrete system will suffer the problem of control period mismatch during similitude analysis if the control gain is improperly high. Control period mismatch is a problem that the scaling ratio of

control period cannot satisfy the constraints. This problem can lead to unstable oscillation of the scaled model such that the prediction ability of traditional similitude analysis is not good. Here, the effect of discretization and control period is considered, and the similitude analysis method will be proposed for the discrete system.

The discrete controller corresponding to the continuous controller is shown in Figure 3. In Figure 3, the equivalent feedback includes the position feedback and velocity feedback, which is equivalently moved forward to the position loop. Let the control period be T, and z should satisfy $z = \mathrm{e}^{-Ts}$.

The following assumptions are made for the system.

(1) The input signal is bandwidth-limited and the sampling time satisfies the Nyquist sampling theorem.

(2) The control period equals the sampling time.

Based on the above assumptions and the design principle of unit impulse response equivalent, the differential calculation is replaced by the following numerical differentier:

$$D(z) = \frac{z-1}{Tz}. \tag{14}$$

Based on eq. (14), the feedforward controller can be written as $F(z) = K_{\mathrm{vff}}\frac{z-1}{Tz}$. The position loop and velocity loop can be expressed as $G_p(z) = K_p$ and $G_v(z) = K_v + TI_v\frac{z}{z-1}$, respectively. Thus, the equivalent feedback can be written as $H(z) = 1 + \frac{z-1}{K_pTz}$. The transfer function from the output of the velocity loop controller to θ can be written in continuous form as

$$G_m(s) = K_t\frac{1-\mathrm{e}^{-Ts}}{J_m s^3}. \tag{15}$$

Setting virtual sampling switch at the output of the controller, the discrete form of the continuous part in eq. (15) can be expressed as

$$G_m(z) = \frac{K_tT^2(z+1)}{2J_m(z-1)^2}. \tag{16}$$

Therefore, the open loop transfer function of the discrete system can be rewritten as

$$G_{\mathrm{op}}(z) = \frac{K_pK_tT^2(z+1)}{2J_m(z-1)^2}\left(K_v + TI_v\frac{z}{z-1}\right)\left(1 + \frac{z-1}{K_pTz}\right). \tag{17}$$

Based on eq. (17), the characteristic equation of the discrete controller can be derived as

$$M(z) = 2J_mz(z-1)^3 + K_pK_tT^2(z+1) \times\left[K_v(z-1) + TI_vz\right]\left(z + \frac{z-1}{K_pT}\right). \tag{18}$$

Assuming that eq. (18) is the characteristic equation of the full-size prototype, the characteristic equation of the scaled model can be expressed as

$$M'(z) = 2\lambda_{Jm}J_mz(z-1)^3 + \lambda_{Kp}\lambda_{KI}\lambda_T^2K_pK_tT^2(z+1) \times\left[\lambda_{Kv}K_v(z-1) + \lambda_T\lambda_{Iv}TI_vz\right]\left(z + \frac{z-1}{\lambda_{Kp}\lambda_TK_pT}\right). \tag{19}$$

The constraints of scaling ratios shown in eqs. (7), (8) and (13) are also effective for the discrete controller. Based on eqs. (18) and (19), it can be obtained that $\lambda_T = \lambda_t$. Since the dimension of z is 1, it can be known from dimensional analysis that the characteristic equations of the full-size prototype and the scaled model have the same roots. Thus, the scaled model will be stable as the full-size prototype if all constraints of scaling ratios can be satisfied.

However, the geometric size of the scaled model is usually smaller than that of the full-size prototype. Namely, $\lambda_1 < 1$. Based on eq. (7), it can be derived that

$$\lambda_T = \lambda_t = \lambda_1^{0.5} < 1. \tag{20}$$

Eq. (20) shows that the control period of the scaled model must be smaller than that of the full-size prototype. It is known that the smaller the control period, the more difficult the controller to be designed. Since the full-size prototype is eventually used in practices, the controller of the full-size prototype is supposed to have a relatively small control period so that the control characteristics can be improved. Under this circumstances, it is difficult to find a controller with short control period satisfying eq. (20) for the scaled model. This problem that the scaling ratio of control period cannot be satisfied is called the problem of control period mismatch.

If the control period mismatch occurs, eq. (20) cannot be

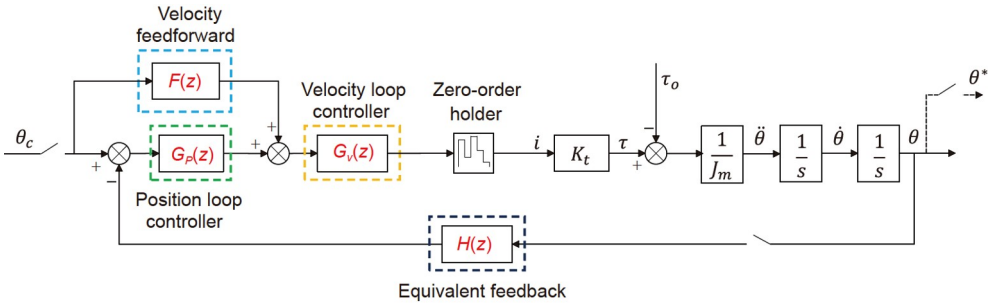

Figure 3 (Color online) Equivalent discrete controller.

satisfied. Thus, the coefficients of eq. (19) will change, and then the distribution of roots of characteristics equation and the stability of the system will be affected. Let the actual scaling ratio of control period be $\hat{\lambda}_T$, and eq. (19) can be rewritten as

$$M'(z) = 2\lambda_{Jm}J_m z(z-1)^3 + \lambda_{Kp}\lambda_{Ki}\lambda_T^2 K_p K_i \left(\frac{\hat{\lambda}_T}{\lambda_T}T\right)^2 (z+1) \times \left[\lambda_{Kv}K_v(z-1) + \lambda_T\lambda_{Iv}\left(\frac{\hat{\lambda}_T}{\lambda_T}T\right)I_v z\right] \times \left(z + \frac{z-1}{\lambda_{Kp}\lambda_T K_p}\frac{\lambda_T}{\hat{\lambda}_T T}\right). \quad (21)$$

Eq. (21) shows that the actual control period of the full-size prototype is $\frac{\hat{\lambda}_T}{\lambda_T}T$. Let $\frac{\hat{\lambda}_T}{\lambda_T}$ be the mismatch level of control period (hereinafter referred to as mismatch level). Based on the definition of scaling ratio, the mismatch level satisfies $\frac{\hat{\lambda}_T}{\lambda_T} \geq 1$. Besides, the worse the mismatch level becomes, the bigger the difference between the actual and desired control periods of the scaled model is. Therefore, this index can reflect the severity of mismatch problem. To reveal the effects of control period mismatch on the similitude analysis, the root locus diagrams of eq. (21) with different control parameters in Table 2 are plotted, as shown in Figure 4. In Figure 4, the black dotted line represents the unit circle, and arrows represent the moving direction of roots. The relationships between the largest modulus length of roots and the control period with different control parameters are shown in Figure 5. The black dotted line represents the unit length. The abscissas of the intersection of each curve and the dotted line are the maximum control period that can guarantee the system stability.

From Figure 4, it can be seen that the position of the largest roots will change when the mismatch level changes. For any control parameters, if the mismatch level is large enough, the roots of the characteristic equation in eq. (21) will eventually exceed the range of unit circle centered on the origin. It illustrates that the control period mismatch affects the stability of the scaled model. In addition, Figure 5 shows that the larger the control gain is, the smaller the control period is when the curve crosses the unit length line. Thus, a relatively small control period is needed when the high control gains are used. Because of this, the scaled model has to work with

Table 2 Value of control parameters

Name of the parameter	The 1st group	The 2nd group	The 3rd group
K_p	100	100	500
K_v	0.8	2	0.8
I_v	67	67	67

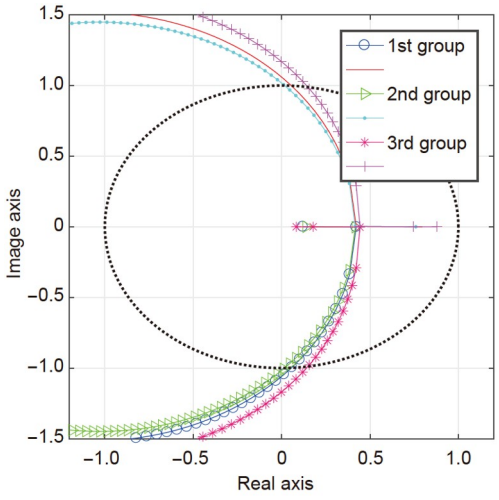

Figure 4 (Color online) The root locus diagrams changing with mismatch level.

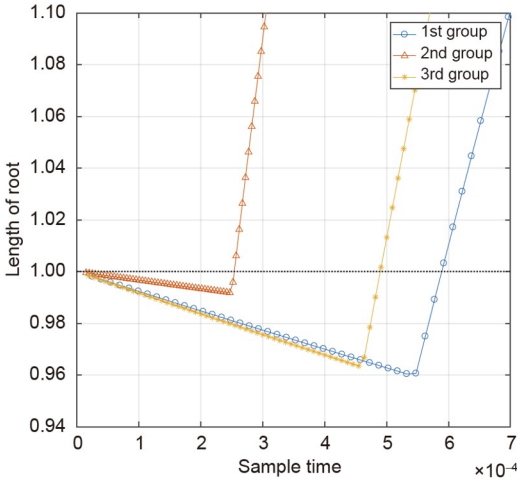

Figure 5 (Color online) The largest modulus length of roots.

low control gains to avoid instability when the control period mismatch occurs. It is obvious that the prediction ability of the scaled model is limited and cannot be fully utilized due to the mismatch problem.

To clearly explain this effect, the ranges of control parameters of the scaled model that can guarantee its stability are plotted in Figure 6. The control period of the scaled model is 0.25, 0.5 and 0.75 ms, respectively. From Figure 6, it can be seen that the range of control parameters decreases with the increase of control period. The difference between different ranges is the loss of prediction ability due to the mismatch problem. In general, the control error will be reduced when the control gain increases. Thus, the control period mismatch problem is particularly significant for the similitude analysis of high-precision electro-mechanical equipment.

For a better illustration of the mismatch problem, the dynamic response of a single axis lifting system is simulated.

The closed-loop feedback control method is adapted and the load on motor axis is a constant gravitational torque. Both the control errors of the full-size prototype and the scaled model with mismatch problem are simulated, as shown in Figure 7. The control periods of the full-size prototype and the scaled model are both 0.1 s. The control period of the scaled model is mismatched since 0.05 s is the desired control period. It can be seen that a mismatch control period can lead to unstable oscillation. Therefore, it is necessary to modify the general similitude analysis method for electro-mechanical performance prediction.

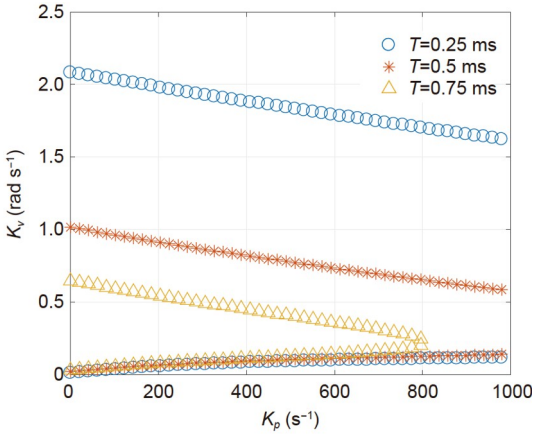

Figure 6 (Color online) The ranges of control parameters guaranteeing stability.

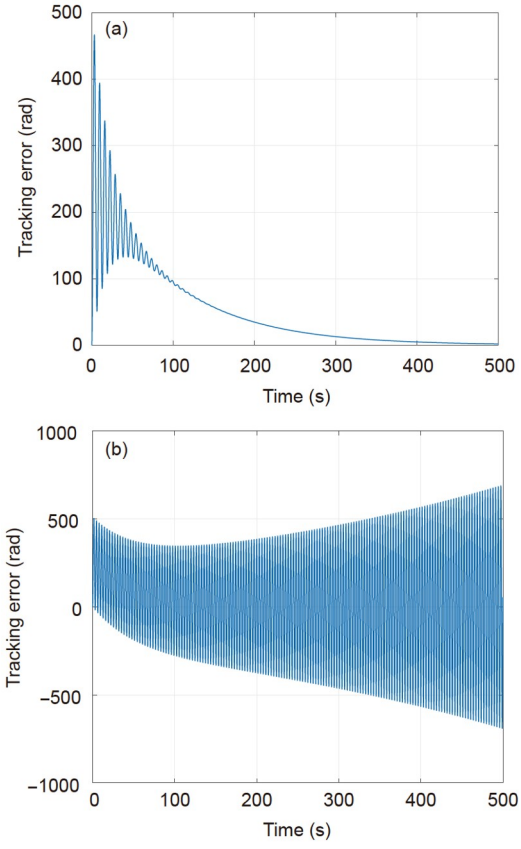

Figure 7 (Color online) Tracking errors of a single axis lifting system. (a) Full-size prototype; (b) scaled model with mismatch problem.

5 The problem of control period mismatch

5.1 Derivation of LPE

For the control period mismatch problem, the control period is so strongly constrained that it is unable to be scaled down according to λ_t. The basic idea to solve this problem is to make λ_t in turn be determined by $\hat{\lambda}_T$. In this case, $\hat{\lambda}_T$ is selected as an independent scaling ratio and the scaling law $\boldsymbol{\pi}_7$ is relaxed to avoid contradiction, thus $\lambda_t = \hat{\lambda}_T$ can always be satisfied. In this way, control period mismatch is transformed into the problem of similitude law relaxation.

5.1.1 Electro-mechanical performance of the system

Since the tracking errors of driven axes can reflect the system performance, they are taken as the performance index to evaluate the electro-mechanical performance. The tracking error denotes the difference between θ^* and θ, which is mainly caused by the controller itself and the external torques. The closed loop transfer function with the input signal θ can be expressed as

$$G_{\mathrm{cl}}(z) = \frac{\left(1+\frac{K_{\mathrm{vff}}}{K_p}\frac{z-1}{Tz}\right)K_pK_tT^2(z+1)[K_v(z-1)+TI_vz]\left(z+\frac{z-1}{K_pT}\right)}{2J_mz(z-1)^3+K_pK_tT^2(z+1)[K_v(z-1)+TI_vz]\left(z+\frac{z-1}{K_pT}\right)}. \quad (22)$$

Based on eq. (22), the tracking error θ_{e1}^* caused by controller itself can be expressed as

$$\theta_{e1}^* = \frac{2J_mz^2(z-1)^3-K_{\mathrm{vff}}K_tT(z^2-1)[K_v(z-1)+TI_vz]\left(z+\frac{z-1}{K_pT}\right)}{2J_mz^2(z-1)^3+K_pK_tT^2z(z+1)[K_v(z-1)+TI_vz]\left(z+\frac{z-1}{K_pT}\right)}\theta_c^*. \quad (23)$$

Let θ_{e2} be the tracking error caused by τ_o. Taking τ_o as the input signal, the feedforward loop from τ_o to θ_{e2} can be expressed as

$$\theta_{e2} = \theta = (\tau-\tau_o)\frac{1}{J_ms^2}. \quad (24)$$

Moreover, the feedback loop from θ to τ can be expressed as

$$\tau = -K_tL_s^z\left(\theta_{e2}^*HG_pG_v\right)\frac{1-\mathrm{e}^{-Ts}}{s}, \quad (25)$$

where $L_s^z(\cdot)$ represents the function that transforms the discrete signal $\cdot$ from z domain to s domain. Based on eqs. (24) and (25), it can be derived that

$$\left(\tau\frac{1}{J_m s^2}\right)^* = -\frac{K_t}{J_m}\left\{L_s^z\left[\left(\tau\frac{1}{J_m s^2}\right)^* HG_pG_v\right]\frac{1-\mathrm{e}^{-Ts}}{s}\frac{1}{s^2}\right\}^* + \frac{K_t}{J_m}\left\{L_s^z\left[\left(\tau_o\frac{1}{J_m s^2}\right)^* HG_pG_v\right]\frac{1-\mathrm{e}^{-Ts}}{s}\frac{1}{s^2}\right\}^*, \quad (26)$$

where the superscript * represents the discretization of a continuous variable. The explicit expression of θ_{e2}^* is expected to be derived from eq. (26). Here, a lemma is introduced to simplify eq. (26) to find θ_{e2}^*.

Lemma 1 A discrete variable $U(n)$ is processed by zero-order holder, double integration and discretization sequentially. The output signal $W(z)$ can be written as

$$W(z) = \frac{T^2(z+1)}{2(z-1)^2}U(z),$$

where $U(z)$ is the z transform of $U(n)$.

Proof $U(n)$ is processed by the zero-order holder and the corresponding continuous signal is $u(t)$. $u(t)$ can be expressed as

$$u(t) = U(n), \quad nT \le t < (n+1)T.$$

Let $v(t)$ be the integration of $u(t)$, and $w(t)$ be the double integration of $u(t)$. At the sampling point, there exists

$$w(nT) = \int_{(n-1)T}^{nT}\int_{(n-1)T}^{t} u(\tau)\mathrm{d}\tau\mathrm{d}t + v[(n-1)T]T + w[(n-1)T].$$

Since $u(t)$ is a constant in $(n-1)T \le t < nT$, the discretization of $w(t)$ can be written as

$$W(n) = U(n-1)\frac{T^2}{2} + V(n-1)T + W(n-1), \quad (27)$$

where $W(n)$ is the discretization of $w(t)$. Taking z transform on eq. (27) leads to

$$W(z) = \frac{T^2 z^{-1}}{2(1-z^{-1})}U(z) + \frac{Tz^{-1}}{1-z^{-1}}V(z). \quad (28)$$

In the same way, the discretization of $v(t)$ can be expressed as

$$V(n) = \int_{(n-1)T}^{nT} u(t)\mathrm{d}t + V(n-1) = U(n-1)T + V(n-1), \quad (29)$$

where $V(n)$ is the discretization of $v(t)$. Taking z transform on eq. (29) yields

$$V(z) = \frac{Tz^{-1}}{1-z^{-1}}U(z). \quad (30)$$

Substituting eq. (30) into eq. (28) leads to

$$W(z) = \frac{T^2(z+1)}{2(z-1)^2}U(z).$$

Proof end.

Based on the lemma, the following equations can be obtained:

$$\left\{L_s^z\left[\left(\tau\frac{1}{J_m s^2}\right)^* HG_pG_v\right]\frac{1-\mathrm{e}^{-Ts}}{s^3}\right\}^* = \frac{T^2(z+1)}{2(z-1)^2}\left(\tau\frac{1}{J_m s^2}\right)^* HG_pG_v,$$
$$\left\{L_s^z\left[\left(\tau_o\frac{1}{J_m s^2}\right)^* HG_pG_v\right]\frac{1-\mathrm{e}^{-Ts}}{s^3}\right\}^* = \frac{T^2(z+1)}{2(z-1)^2}\left(\tau_o\frac{1}{J_m s^2}\right)^* HG_pG_v. \quad (31)$$

Substituting eq. (31) into eq. (26) yields

$$\left(\tau\frac{1}{J_m s^2}\right)^* = \frac{K_t T^2(z+1)HG_pG_v}{2J_m(z-1)^2 + K_t T^2(z+1)HG_pG_v}\left(\tau_o\frac{1}{J_m s^2}\right)^*. \quad (32)$$

Based on eq. (32), θ_{e2}^* can be expressed as

$$\theta_{e2}^* = -\frac{2J_m z(z-1)^3\left(\tau_o\frac{1}{J_m s^2}\right)^*}{2J_m z(z-1)^3 + K_p K_t T^2(z+1)[K_v(z-1)+TI_v z]\left(z+\frac{z-1}{K_p T}\right)}, \quad (33)$$

where $\tau_o\frac{1}{J_m s^2}$ represents the angular output caused by external torque without a controller. Let $\theta_{\tau o} = \tau_o\frac{1}{J_m s^2}$ and the discrete form of $\theta_{\tau o}$ be $\theta_{\tau o}^*$. Based on eqs. (23) and (33), the total tracking error θ_e^* can be written as

$$\theta_e^* = \theta_{e1}^* + \theta_{e2}^* = G_{q1}(z)\theta_c^* + G_{q2}(z)\theta_{\tau o}^*, \quad (34)$$

where

$$G_{q1}(z) = \frac{2J_m z^2(z-1)^3 - K_{\mathrm{vff}}K_t T(z^2-1)[K_v(z-1)+TI_v z]\left(z+\frac{z-1}{K_p T}\right)}{2J_m z^2(z-1)^3 + K_p K_t T^2 z(z+1)[K_v(z-1)+TI_v z]\left(z+\frac{z-1}{K_p T}\right)},$$

$$G_{q2}(z) = -\frac{2J_m z(z-1)^3}{2J_m z(z-1)^3 + K_p K_t T^2(z+1)[K_v(z-1)+TI_v z]\left(z+\frac{z-1}{K_p T}\right)}.$$

5.1.2 *Effect of relaxation problem and LPE*

The effects of relaxing $\boldsymbol{\pi}_7$ can be concluded from eq. (34). Based on the theory of similitude analysis, the scaling ratios of $G_{q1}(z)$, θ_c^* and $G_{q2}(z)$ will not be affected by the relaxation of $\boldsymbol{\pi}_7$ since $\lambda_t = \hat{\lambda}_T$ is always satisfied. However, for $\theta_{\tau o}^*$, the moment of inertia and the moment of gravity will have different scaling ratios due to the relaxation of $\boldsymbol{\pi}_7$. Meanwhile, the coulomb and viscous friction coefficients of the scaled model will not change with λ_t. Thus, the scaling ratios of the two kinds of friction moments will also be different. Since the components of τ_o have different scaling ratios, $\theta_{\tau o}^*$ is no longer scaled down with a constant scaling ratio, and the similitude analysis on θ_e^* cannot be properly carried out. This

is the effects of relaxation problem.

To solve this problem, $\theta_{\tau o}$ is furtherly decomposed as

$$\theta_{\tau o} = {}^{g}\theta_{\tau o} + {}^{v}\theta_{\tau o} + {}^{a}\theta_{\tau o}, \tag{35}$$

where ${}^{g}\theta_{\tau o}$ is the angular output caused by the moment of gravity and the moment of coulomb friction, and ${}^{v}\theta_{\tau o}$ and ${}^{a}\theta_{\tau o}$ are the angular outputs caused by the moment of viscous friction and the moment of inertia, respectively.

The components in eq. (35) have the following relationships:

$${}^{g}\theta'_{\tau o} \propto \lambda_t^{2},\ {}^{v}\theta'_{\tau o} \propto \lambda_t,\ {}^{a}\theta'_{\tau o} \propto \lambda_t^{0}, \tag{36}$$

where ${}^{g}\theta'_{\tau o}$, ${}^{v}\theta'_{\tau o}$ and ${}^{a}\theta'_{\tau o}$ are the value of ${}^{g}\theta_{\tau o}$, ${}^{v}\theta_{\tau o}$ and ${}^{a}\theta_{\tau o}$ in the scaled model. ${}^{g}\theta'_{\tau o}$ and ${}^{v}\theta'_{\tau o}$ are proportional to the square of λ_t^{2} and λ_t, respectively. ${}^{a}\theta'_{\tau o}$ is not affected by λ_t. For the same scaled model, several different ${}^{i}\lambda_t$ and ${}^{i}\widehat{\lambda}_T$ are given and the following condition should be satisfied:

${}^{i}\lambda_t = {}^{i}\widehat{\lambda}_T \geq 1$.

On the one hand, based on eqs. (8), (10) and (13), the scaling ratios of all other parameters can be determined when ${}^{i}\lambda_t = {}^{i}\widehat{\lambda}_T$. The scaled down experiments with ${}^{i}\lambda_t$ can then be carried out in sequence, and the corresponding tracking error of the scaled model ${}^{i}\theta_e^{*\prime}$ can be obtained. On the other hand, ${}^{i}\theta_e^{*\prime}$ can also be expressed as

$$\begin{aligned} {}^{i}\theta_e^{*\prime} = {}&{}^{i}\lambda_\theta\,{}^{i}\lambda_{G1}G_{\theta 1}(z)\theta_c^{*} + {}^{i}\lambda_{\theta g}\,{}^{i}\lambda_{G2}G_{\theta 2}(z)\,{}^{g}\theta_{\tau o}^{*} \\ &+ {}^{i}\lambda_{\theta v}\,{}^{i}\lambda_{G2}G_{\theta 2}(z)\,{}^{v}\theta_{\tau o}^{*} + {}^{i}\lambda_{\theta a}\,{}^{i}\lambda_{G2}G_{\theta 2}(z)\,{}^{a}\theta_{\tau o}^{*}, \end{aligned} \tag{37}$$

where ${}^{i}\lambda_{\theta a}$, ${}^{i}\lambda_{\theta v}$ and ${}^{i}\lambda_{\theta g}$ are the scaling ratios of ${}^{a}\theta_{\tau o}$, ${}^{v}\theta_{\tau o}$ and ${}^{g}\theta_{\tau o}$ corresponding to ${}^{i}\lambda_t$, and ${}^{i}\lambda_{G1}$ and ${}^{i}\lambda_{G2}$ are scaling ratios of $G_{\theta 1}(z)$ and $G_{\theta 2}(z)$ corresponding to ${}^{i}\lambda_t$. Based on the dimensional analysis, it can be derived that

$${}^{i}\lambda_{G1} = {}^{i}\lambda_{G2} = 1,\ {}^{i}\lambda_{\theta} = {}^{i}\lambda_{\theta a} = 1,\ {}^{i}\lambda_{\theta v} = {}^{i}\lambda_t,\ {}^{i}\lambda_{\theta g} = {}^{i}\lambda_t^{2}. \tag{38}$$

Based on eq. (38), eq. (37) can be simplified as

$$\mathbf{A}_\lambda \boldsymbol{\theta}^{*} = \boldsymbol{\theta}_{e'}^{*}, \tag{39}$$

where $\mathbf{A}_\lambda$ is the coefficient matrix. The ith row ${}^{i}\mathbf{A}_\lambda$ of $\mathbf{A}_\lambda$ can be expressed as

$${}^{i}\mathbf{A}_\lambda(z) = \left[1 \quad {}^{i}\lambda_t \quad {}^{i}\lambda_t^{2}\right].$$

Besides, $\boldsymbol{\theta}^{*}$ and $\boldsymbol{\theta}_{e'}^{*}$ can be expressed as

$$\boldsymbol{\theta}^{*} = \left[G_{\theta 1}(z)\theta_c^{*} + G_{\theta 2}(z)\,{}^{a}\theta_{To}^{*} \quad G_{\theta 2}(z)\,{}^{g}\theta_{To}^{*} \quad G_{\theta 2}(z)\,{}^{v}\theta_{To}^{*}\right]^{\mathrm{T}},$$

$$\boldsymbol{\theta}_{e'}^{*} = \left[{}^{1}\theta_e^{*\prime} \quad \cdots \quad {}^{\xi}\theta_e^{*\prime}\right]^{\mathrm{T}},$$

where ξ is the amount of experiments. Since θ_c^{*}, ${}^{a}\theta_{To}^{*}$, ${}^{g}\theta_{To}^{*}$ and ${}^{v}\theta_{To}^{*}$ are all unknowns, $\boldsymbol{\theta}^{*}$ is the unknown vector that need to be solved. It can be seen that eq. (39) is a system of linear equations related to $\boldsymbol{\theta}_{e'}^{*}$. If $\xi \geq 3$, based on the least square principle, $\boldsymbol{\theta}^{*}$ can be uniquely solved as

$$\boldsymbol{\theta}^{*} = \mathbf{A}_\lambda^{+}\boldsymbol{\theta}_{e'}^{*},$$

where $\mathbf{A}_\lambda^{+}$ is the Moore-Penrose inverse of $\mathbf{A}_\lambda$. Based on the superposition principle of linear system, θ_e^{*} can be predicted as

$$\theta_e^{*} = [1 \quad 1 \quad 1]\boldsymbol{\theta}^{*} = [1 \quad 1 \quad 1]\mathbf{A}_\lambda^{+}\boldsymbol{\theta}_{e'}^{*}. \tag{40}$$

Eq. (40) is the general formulation of LPE. It can be seen that in LPE, the relaxation of $\boldsymbol{\pi}_7$ no longer affects the prediction of tracking error at the expense of increasing the amount of experiment. Therefore, the problem of control period mismatch can be eventually solved.

5.2 Prediction deviation of LPE

In the LPE, τ_o is simplified and the unmodeled external disturbance is neglected. Here, the prediction deviation caused by the unmodeled disturbance is analyzed to figure out the error of LPE in actual condition. The prediction deviation can be expressed as

$$\Delta\theta_e^{*} = \tilde{\theta}_e^{*} - \hat{\theta}_e^{*},$$

where $\hat{\theta}_e^{*}$ is the actual tracking error of the full-size prototype, and $\tilde{\theta}_e^{*}$ is the tracking error predicted by LPE. Since the velocity feedforward and closed-loop feedback system is linear, $\hat{\theta}_e^{*}$ can be expressed as

$$\hat{\theta}_e^{*} = \hat{\theta}_{e0}^{*} + \Delta\hat{\theta}_{e0}^{*},$$

where $\hat{\theta}_{e0}^{*}$ is the tracking error of the full-size prototype without unmodeled disturbance, and $\Delta\hat{\theta}_{e0}^{*}$ is the tracking error caused by unmodeled disturbance. $\tilde{\theta}_e^{*}$ can also be expressed as

$$\tilde{\theta}_e^{*} = \theta_e^{*} + \Delta\tilde{\theta}_{e0}^{*},$$

where θ_e^{*} is the predicted tracking error without unmodeled disturbance, and $\Delta\tilde{\theta}_{e0}^{*}$ is the prediction deviation caused by disturbance in the scaled model. It is obvious that $\theta_e^{*} = \hat{\theta}_{e0}^{*}$. Thus, $\Delta\theta_e^{*} = \Delta\tilde{\theta}_{e0}^{*} - \Delta\hat{\theta}_{e0}^{*}$ and $\Delta\hat{\theta}_{e0}^{*}$ can be written as

$$\Delta\hat{\theta}_{e0}^{*} = G_{\theta 2}(z)\theta_\omega^{*}, \tag{41}$$

where θ_ω^{*} is the unmodeled disturbance in the full-size prototype. Moreover, if there is disturbance in the scaled model, eq. (41) can be rewritten as ${}^{i}\theta_e^{*\prime} - G_{\theta 2}(z)\,{}^{i}\theta_\omega^{*\prime} = {}^{i}\mathbf{A}_\lambda\boldsymbol{\theta}^{*}$. Thus, the unmodeled disturbance can be equivalent to the measurement error of $\boldsymbol{\theta}_{e'}^{*}$. It can be derived that

$$\frac{\|\Delta\boldsymbol{\theta}^{*}\|}{\|\boldsymbol{\theta}^{*}\|} \leq \mathrm{cond}(\mathbf{A}_\lambda)\frac{\|G_{\theta 2}(z)\boldsymbol{\theta}_{\omega'}^{*}\|}{\|\boldsymbol{\theta}_{e'}^{*}\|}.$$

Considering that $|\Delta\hat{\theta}_{e0}^{*}| = |[1 \quad 1 \quad 1]\Delta\boldsymbol{\theta}^{*}| \leq \|\Delta\boldsymbol{\theta}^{*}\|_1$, the upper

bound of $\left|\Delta\tilde{\theta}_{e0}^{*}\right|$ can be expressed as

$$\left|\Delta\tilde{\theta}_{e0}^{*}\right| \le \mathrm{cond}_1(\mathbf{A}_\lambda)\frac{\left\|G_{\theta 2}(z)\boldsymbol{\theta}_{\omega}^{*\prime}\right\|_1}{\left\|\boldsymbol{\theta}_{e}^{*\prime}\right\|_1}\left\|\boldsymbol{\theta}^{*}\right\|_1. \tag{42}$$

Combining eqs. (41) and (42) leads to

$$\left|\Delta\theta_{e}^{*}\right| \le \left|G_{\theta 2}(z)\theta_{\omega}^{*}\right| + \mathrm{cond}_1(\mathbf{A}_\lambda)\frac{\left\|G_{\theta 2}(z)\boldsymbol{\theta}_{\omega}^{*\prime}\right\|_1}{\left\|\boldsymbol{\theta}_{e}^{*\prime}\right\|_1}\left\|\boldsymbol{\theta}^{*}\right\|_1. \tag{43}$$

From eq. (43), it can be concluded that the prediction deviation is determined by both the unmodeled disturbance and condition number of $\mathbf{A}_\lambda$. The unmodeled disturbance can be reduced by improving the manufacturing and assembling accuracy and lubricating condition. The effects of condition number of $\mathbf{A}_\lambda$ can be decreased by properly selecting ${}^{i}\lambda_t$. It should be noticed that motors might work in low speed condition if ${}^{i}\lambda_t$ is too big, and this may lead to non-ideal factors such as squirming and crawling. Therefore, ${}^{i}\widehat{\lambda}_T$ need to be properly specified to minimize the prediction deviation.

6 The problem of control period mismatch

The full-size heavy-duty hybrid machine tool is about 6.6 m in height, and the scaled model is 1:5 on the size of the full-size prototype. Thus, $\lambda_x = 0.2$. The motor of the scaled model is selected with $\lambda_{Kt} = 0.588$. Based on the similitude analysis, the scaled model of the full-size prototype is built, as shown in Figure 8.

To validate the effectiveness of LPE, the actual tracking errors of the full-size parallel manipulator and the tracking errors predicted by LPE method are compared. The full-size heavy-duty hybrid machine tool has been built for a long time and now it cannot work. Since the traditional method is proved to be accurate enough in low gain condition [22], the tracking error of the full-size prototype with proper control gains obtained by the traditional method is regarded as the real tracking errors, which is called 'reference error'. Meanwhile, the tracking errors obtained by LPE method are called 'predicted error'.

The moving platform of the full-size prototype is expected to move along two periodic trajectories and the key points in the two trajectories are shown in Table 3. Line trajectory and trapezoidal acceleration are used between different key points. The maximum acceleration of the moving platform is

Figure 8 (Color online) The scaled model.

2 m s^{-2}, and the maximum velocity is 134 mm s^{-1}.

Based on the direct similitude analysis, it can be obtained that $\lambda_t = \lambda_x^{0.5} \approx 0.447$, while in LPE method, let ${}^{i}\lambda_t$ get the values from the set $\lambda_t \in \{0.531 \quad 0.632 \quad 0.751 \quad 0.894\}$. The tracking errors of the two axes of the parallel manipulator in the scaled model are measured, and the reference and predicted errors of the full-size prototype are obtained based on eqs. (13) and (40), as shown in Figures 9 and 10. For convenience, the normalized time which is the ratio of time to the period of the trajectory is used. In Figure 9, since the peak of tracking errors and the peak of acceleration/deceleration occur at the same time, the peak errors are mainly caused by the high acceleration/deceleration during reversing and start-stop process. Besides, the tracking error in constant speed stage is periodic and the periods change between different key points of the trajectory. This is the result of periodic disturbance caused by coaxiality between the motor and the ball screw, and the tacking errors have the same periods as the disturbance. It can be seen from Figure 9 that the shape of reference and predicted errors are basically the same, and the peak value occurs at the same time. It shows that LPE can properly reflect the inner principle of electro-mechanical process. Moreover, the peak value of the reference errors is less than 0.65°, which reflects a relatively good tracking performance. The average prediction deviations of the peak tracking errors in trajectory 1 are 8.15% and 10.78% of the two axes of the parallel manipulator, respectively.

Compared with trajectory 1 whose key points are randomly distributed, trajectory 2 is a rectangle trajectory, so that the periods of tracking errors in constant speed stage are closer. The average prediction deviations of the peak track-

Table 3 Key point of the trajectory

	Key point 1	Key point 2	Key point 3	Key point 4	Key point 5	Key point 6	Key point 7
Trajectory 1 (mm)	(0, 0)	(50, 100)	(−50, 75)	(25, 125)	(−40, 70)	(10, 25)	(0, 0)
Trajectory 2 (mm)	(0, 0)	(50, 0)	(50, 100)	(−50, 100)	(−50, 0)	(0, 0)	–

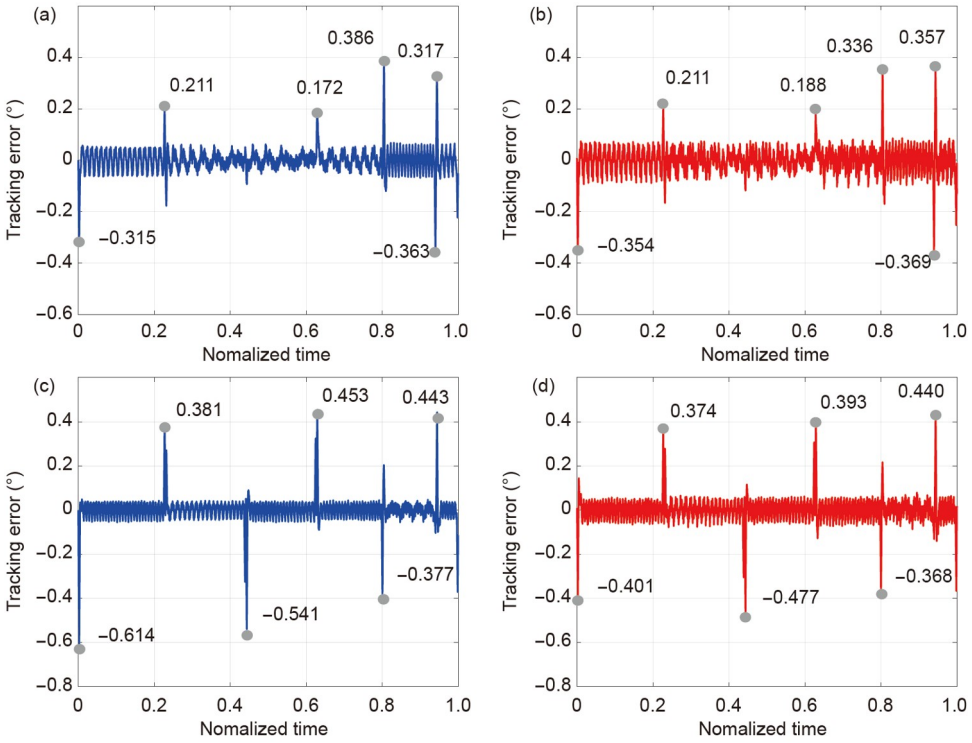

Figure 9 (Color online) Tracking errors in trajectory 1. (a) Reference error of axis 1; (b) predicted error of axis 1; (c) reference error of axis 2; (d) predicted error of axis 2.

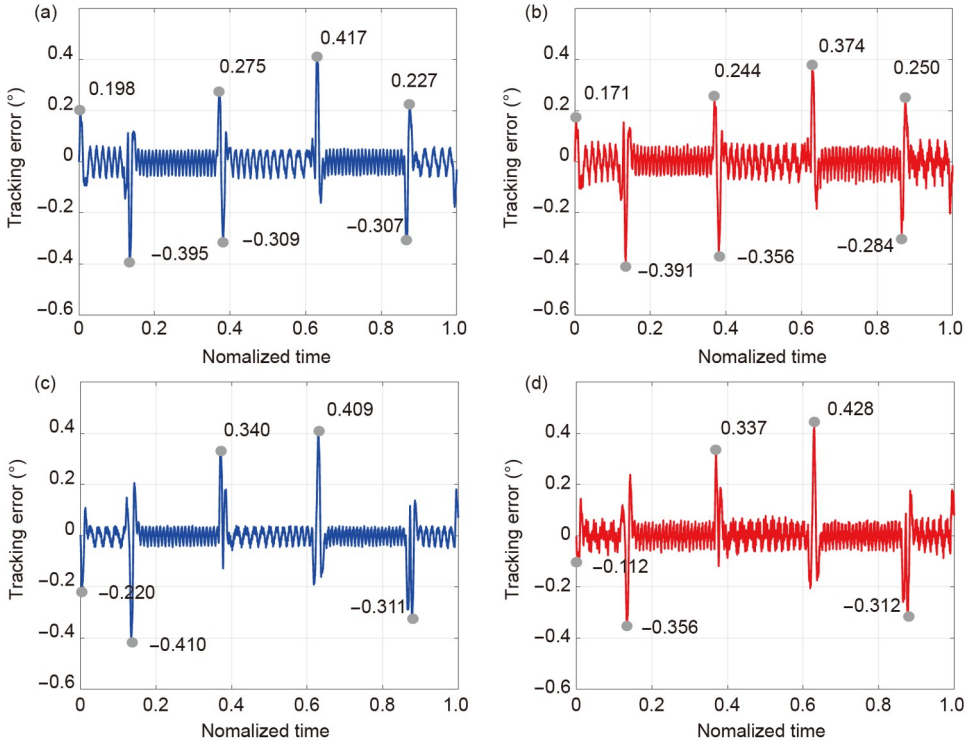

Figure 10 (Color online) Tracking errors in trajectory 2. (a) Reference error of axis 1; (b) predicted error of axis 1; (c) reference error of axis 2; (d) predicted error of axis 2.

ing errors in trajectory 2 are 9.87% and 13.62%, respectively. The prediction accuracy of LPE can meet the requirement of many applications. Furthermore, the reference and predicted tracking errors of the moving platform are also plotted based on the error of each axis and direct kinematics, as shown in Figure 11. It can be seen that the tracking errors are less than

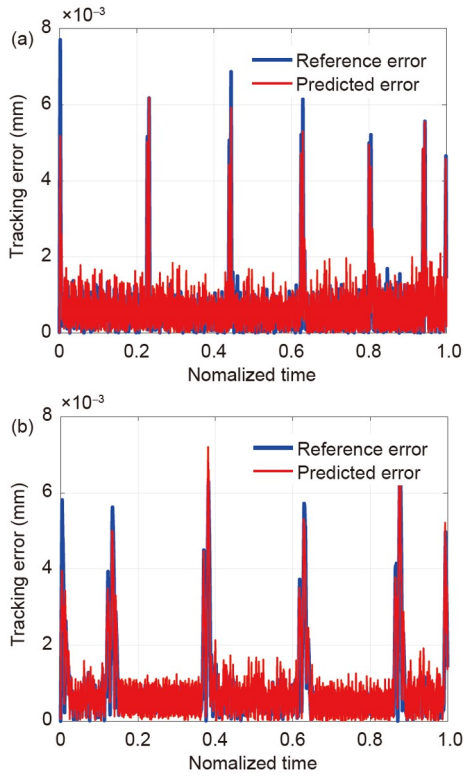

Figure 11 Reference and predicted tracking errors of the moving platform. (a) Trajectory 1; (b) trajectory 2.

8×10^{-3} mm for both trajectories, and the predicted errors coincide well with the reference errors. Therefore, the effectiveness of LPE is validated. Since LPE is derived by considering the discretization of controller, other performances such as positioning accuracy and contour error can also be predicted by this method.

7 Conclusion

In this paper, a modified similitude analysis method to predict the electro-mechanical performances of the parallel manipulator in a hybrid machine tool is proposed, and the problem of control period mismatch is investigated. The traditional method which regards the controller as continuous system is used to derive the similitude laws related to electro-mechanical performances. Then the effects of control period mismatch are figured out by establishing the discrete form of the controller characteristics. The long period equivalent method is proposed to solve the mismatch problem. Finally, the scaled down experiments of the parallel manipulator are carried out, and the tracking errors of the full-size prototype are predicted by both traditional similitude analysis and long period equivalent method. The deviations are less than 11% and 14% for the two trajectories, respectively. This method can also be extended for the similitude analysis of other electro-mechanical performances when the control period mismatch problem occurs.

This work was supported by the National Natural Science Foundation of China (Grant No. 51975321) and the Opening Project of the Key Laboratory of CNC Equipment Reliability, Ministry of Education, Jilin University (Grant No. 202101).

1 Wu J, Yu G, Gao Y, et al. Mechatronics modeling and vibration analysis of a 2-DOF parallel manipulator in a 5-DOF hybrid machine tool. Mechanism Machine Theor, 2018, 121: 430–445
2 Son S, Kim T, Sarma S E, et al. A hybrid 5-axis CNC milling machine. Precision Eng, 2009, 33: 430–446
3 Wu J, Zhang B B, Wang L P, et al. An iterative learning method for realizing accurate dynamic feedforward control of an industrial hybrid robot. Sci China Tech Sci, 2021, 64: 1177–1188
4 Liu H T, Huang T, Kecskeméthy A, et al. A generalized approach for computing the transmission index of parallel mechanisms. Mech Mach Theor, 2014, 74: 245–256
5 Bi Z M. Kinetostatic modeling of Exechon parallel kinematic machine for stiffness analysis. Int J Adv Manuf Technol, 2014, 71: 325–335
6 Dong C L, Liu H T, Yue W, et al. Stiffness modeling and analysis of a novel 5-DOF hybrid robot. Mech Mach Theor, 2018, 125: 80–93
7 Caccavale F, Siciliano B, Villani L. The tricept robot: Dynamics and impedance control. IEEE/ASME Trans Mech, 2003, 8: 263–268
8 Yang X J, Lu D, Liu H, et al. Electromechanical integrated modeling and analysis for the direct-driven feed system in machine tools. Int J Adv Manuf Technol, 2018, 98: 1591–1604
9 Yang X J, Lu D, Zhang J, et al. Dynamic electromechanical coupling resulting from the air-gap fluctuation of the linear motor in machine tools. Int J Mach Tools Manu, 2015, 94: 100–108
10 Brecher C, Weck M, Yamasaki T. Controller-integrated predictive oscillation compensation for machine tools with parallel kinematics. Int J Mach Tools Manu, 2005, 46: 142–150
11 Wu Q H, Sun Y Z, Chen W Q, et al. An mechatronics coupling design approach for aerostatic bearing spindles. Int J Precis Eng Manu, 2019, 20: 1185–1196
12 Yin F W, Tian W J, Liu H T, et al. A screw theory based approach to determining the identifiable parameters for calibration of parallel manipulators. Mech Mach Theor, 2020, 145: 103665
13 Wu J, Wang J S, You Z. An overview of dynamic parameter identification of robots. Robot Comput-Integrated Manu, 2010, 26: 414–419
14 Xu T. A Similar Method and Its Application (in Chinese). Beijing: China Machine Press, 1995
15 Vassalos D. Physical modelling and similitude of marine structures. Ocean Eng, 1998, 26: 111–123
16 Browne M T L, Taylor Z J, Li S, et al. A wind load design method for ground-mounted multi-row solar arrays based on a compilation of wind tunnel experiments. J Wind Eng Ind Aerod, 2020, 205: 104294
17 Sabour M H, Bhat R B. Thermal scale modeling by FEM and test. J Aerosp Eng, 2010, 23: 24–33
18 Cestino E, Frulla G, Perotto E, et al. Experimental slender wing model design by the application of aeroelastic scaling laws. J Aerosp Eng, 2014, 27: 112–120
19 Kenan H, Azeloğlu O. Design of scaled down model of a tower crane mast by using similitude theory. Eng Struct, 2020, 220: 110985
20 Dewi D K, Abidin Z, Budiwantoro B, et al. Dimensional analysis of a rotor system through FRF using transfer function and finite element methods. J Mech Sci Technol, 2020, 34: 1863–1870
21 Guo H, Zhou T, Xu J Q. Non-proportionally scaled-down model approach to solar array drive system performance prediction considering control strategy. IEEE Access, 2018, 6: 50323–50332
22 Song Y Y, Wu J, Yu G, et al. Dynamic characteristic prediction of a 5-DOF hybrid machine tool by using scale model considering the geometric distortion of bearings. Mech Mach Theor, 2020, 145: 103679